Journal of Power Sources 196 (2011) 8909–8917

Contents lists available at ScienceDirect

Journal of Power Sources

journal homepage: www.elsevier.com/locate/jpowsour

Design of experiment approach applied to reducing and oxidizing tolerance of anode supported solid oxide fuel cell. Part II: Electrical, electrochemical and microstructural characterization of tape-cast cells

Antonin Faes[a,b,*], Zacharie Wuillemin[c], Pietro Tanasini[b,d], Nicola Accardo[a], Stefano Modena[c], Hans J. Schindler[e], Marco Cantoni[a], Henning Lübbe[b,f], Stefan Diethelm[b], Aïcha Hessler-Wyser[a], Jan Van herle[b]

[a] Interdisciplinary Centre for Electron Microscopy (CIME), Ecole Polytechnique Fédérale de Lausanne (EPFL), CH-1015 Lausanne, Switzerland
[b] Industrial Energy Systems Laboratory (LENI), EPFL, CH-1015 Lausanne, Switzerland
[c] SOFCPOWER S.r.l., Pergine Vals., Italy
[d] Group of Electrochemical Engineering (GGEC), EPFL, CH-1015 Lausanne, Switzerland
[e] High Performance Ceramics, EMPA, CH-8600 Dübendorf, Switzerland
[f] Powder Technology Laboratory (LTP), EPFL, CH-1015 Lausanne, Switzerland

ARTICLE INFO

Article history:
Received 20 July 2010
Received in revised form
24 November 2010
Accepted 29 November 2010
Available online 4 December 2010

Keywords:
RedOx cycling
SOFC reoxidation
Solid oxide fuel cells
Ni–YSZ anode support
Cermet electrical conductivity
Degradation

ABSTRACT

One of the major limitations of the nickel (Ni) – yttria-stabilized zirconia (YSZ) anode support for solid oxide fuel cells (SOFC) is its low capability to withstand transients between reducing and oxidizing atmospheres ("RedOx" cycle), owing to the Ni-to-NiO volume expansion. This work presents results on different anode supports fabricated by tape casting. Three compositions are prepared, as the outcome of a preceding design of experiment approach. The NiO proportion is 40, 50 and 60 wt% of the anode composite.

The anode support characteristics like shrinkage during sintering, *in-situ* conductivity at high temperature, electrochemical performance and tolerance against RedOx cycles have been measured. Performance up to 0.72 W cm^{-2} (0.62 V, 800 °C) is recorded for the 60 wt% NiO sample on small cells. The open circuit voltage is maintained within ±5 mV after 10 full RedOx cycles at 800 °C and one at 850 °C. Performances tend to be stabilized after one or multiple RedOx cycles. The microstructural observations show round Ni particles after the first reduction; after a RedOx cycle, the Ni particles include micro-porosities that are stable under humidified reducing atmosphere for more than 300 h.

1. Introduction

The state-of-the-art solid oxide fuel cells anode is based on nickel and a ceramic with high ionic conductivity. Nickel is used because of its high catalytic activity and relative low cost. One of its drawbacks is its sensitivity to reoxidation at SOFC working temperature (600–1000 °C) if air reaches the anode side (lack of fuel, start-up and shut-down of the stack, seal leakage [1], electrolyte cracks [2,3]) or at high fuel utilization [1,4]. This reoxidation is followed by a volume increase of around 71% and a change in NiO microstructure. The reoxidized NiO grains show internal porosity, which reinforces the volume increase. Some groups have demonstrated stability during RedOx cycling for electrolyte-supported cells [5,6]. The limitation of electrolyte-supported cells (ESC) is their high ohmic loss at reduced temperature (700–800 °C) compared to anode-supported cells (ASC). ASC are more sensitive to RedOx cycling than ESC as shown by Sarantaridis and Atkinson [7]: the maximal linear expansion before cracking or buckling is 5 times smaller for ASC (0.2%) compared to ESC (1%). This is the reason why the degradation of ASC after a RedOx cycle is total (cell broken) or in the better case relatively high [8,9].

The goal of this work is to produce anode supports by tape-casting with an optimized composition based on a preceding approach: the optimization work was carried out in part I using design of experiment and response surface methodology; it minimizes RedOx expansion, and maximizes electrical conductivity and sinterability [10]. In the present work, three different sample compositions were fabricated, tested and compared with respect to their electrochemical performance, RedOx stability and electrical conductivity. The particularity is the important variation in NiO

* Corresponding author at: Industrial Energy Systems Laboratory (LENI), Ecole Polytechnique Fédérale de Lausanne (EPFL), MEA2 435 Station 9, CH-1015 Lausanne, Switzerland. Tel.: +41 21 693 6813; fax: +41 21 693 3502.
E-mail address: antonin.faes@a3.epfl.ch (A. Faes).

0378-7753/$ – see front matter © 2010 Elsevier B.V. All rights reserved.
doi:10.1016/j.jpowsour.2010.11.146

Table 1
Composition of the different samples produced by tape-casting. Theses compositions were defined from optimization work presented in [10].

	Tape T40	Tape T50	Tape T60
NiO/wt% in ceramic powder	40	50	60
Pore-former/wt%	3	7.5	9
NiO powder	Fine	95 wt% fine–5 wt% coarse	Fine
YSZ powder	5 wt% fine–95 wt% coarse	5 wt% fine–95 wt% coarse	5 wt% fine–95 wt% coarse

content (40–60 wt%), while maintaining RedOx tolerance and electrochemical performance.

2. Experimental

2.1. Cell preparation

Anode and electrolyte were prepared by water-based tape-casting technology [11]. 8 mol% Y_2O_3 in ZrO_2 (8YSZ) powder from Tosoh® is used for the thin electrolyte; a mixture of NiO, 8YSZ and pore-former is used for the anode-support. The composition of the three different tapes is given in Table 1. For the anode, the ceramic powders, pore-former, water and dispersant (Darvan 821A, R.T. Vanderbilt Inc., USA) were mixed with zirconia balls on a rotatory ball-milling stage for 24 h. The electrolyte suspension was milled 2h30 in a Turbula mixer with zirconia balls (same proportions than for the anode mix). After filtering (anode slurry with 100 μm and electrolyte slurry with 41 μm filters from Millipore) the suspension is degassed and an acrylic binder (Duramax B1000, Rohm et Haas, France) is added. The slurry is stirred during 30 min before tape-casting. The casting was done at 1 cm s^{-1} with a polytetrafluoroethylene double doctor-blade (Mistler, Yardley, USA) on a tape-cast plan (Netzsch-Type634.0, Germany). The doctor-blade gap is 40 μm for the electrolyte and 950 μm for the anode support. Green half-cells are obtained by casting the anode on the dried electrolyte tape. The green tape is cut in discs of 5 cm in diameter. The firing was done with the half-cells (electrolyte on top) in between two sinter support plates 4 h at 1400 °C (Nabertherm HT10/18, Germany).

The cathode is prepared in the way described in [12]; 50:50% in volume of LSM ($(La_{0.75}Sr_{0.25})_{0.95}MnO_{3-d}$, Praxair, Inc., USA) and 8YSZ (Tosoh Corp., Japan). An ink was obtained by adding 3.2 wt% of ethylcellulose in terpineol (powder–solvent ratio 1.36). The cathode is deposited by screen-printing. Two layers of LSM/YSZ were deposited before firing 1 h at 1050 °C. A current collection layer of LSC ($La_{0.5}Sr_{0.5}CoO_{3-x}$, Praxair, Inc.) is screen-printed on top of the LSM/YSZ fired cathode. The final cathode size is 1.0 ± 0.1 cm^2 and is taken to correspond to the active cell area.

2.2. Cell testing

Cell testing is done at 800 °C in a furnace (Rohde, Germany) with a Bentrup TC 505 temperature controller. Before mounting the cell, an anode current collection layer containing 90 wt% NiO (J.T. Baker, Inc., USA) and 10 wt% 8YSZ (Tosoh, Japan) was deposited with a brush on the anode surface. The cells are connected with platinum and nickel meshes to the cathode and the anode, respectively. The temperature is controlled by a K thermocouple placed near the cathode in contact with the electrolyte. The cell was mounted between two alumina felts in a metallic setup pressed with calibrated springs. The gases arrive at the center of the cell with 450 ml min^{-1} of air for the cathode and 300 ml min^{-1} of humidified hydrogen (around 3% H_2O) for the anode. The gases are post-combusted around the cells.

Polarization of the cells was done in galvanostatic mode with an Amel 555b potentiostat–galvanostat. Measurements were done in a four-wire configuration. Potential difference, current and temperature data are acquired and stored in a computer via a Fluke Hydraseries® multichannel device. Electrochemical impedance spectroscopy (EIS) measurements and current–voltage curves were performed with an Eco Chemie Autolab®.

A RedOx cycle procedure is as follows: purging the anode with 500 ml min^{-1} of Ar until the potential reaches 0.7 V (around 10 min), then turning off the argon flow and letting the cell voltage reach 0.02 V (about 20 min), finally flushing the anode with 200 ml min^{-1} of air for minimum 1 h. From thermogravimetric analysis (TGA), it had been established that full oxidation is completed in less than 60 min at 800 °C for these anode supports. The reduction was done by purging the anode with 500 ml min^{-1} argon until the potential reaches 0.09 V, then changing to hydrogen within one minute.

The cells were reduced at 800 °C and polarized for a while; then 10 RedOx cycles at 800 °C were applied. After this the cells were polarized again and a final RedOx cycle applied at 850 °C. After this last measurement the cell was cooled under 10% H_2 in nitrogen.

The area specific resistance (ASR) is given by a linear approximation of the current–voltage (I–V) curve between 0.65 and 0.85 V [13]. Electrochemical measurements were done 1 h after the reduction or re-reduction when not stated otherwise.

To compare microstructures after aging, the as-sintered and tested cells (after electrochemical test) were soaked in a tubular furnace (Lenton, UK) at 800 °C during 300 h under humidified form gas (10% H_2 in nitrogen).

2.3. Conductivity measurements

Conductivity measurements were done by the van der Pauw technique [14,15] on half-cell discs of 4.3 cm in diameter. The contacts were made of nickel foam of 2 by 2 mm^2 welded with platinum wires. To ensure a good contact with the cell, the Ni foam was impregnated with the anode current collecting layer (see Section 2.1). The cell was then mounted in a similar setup than for the electrochemical test (see Section 2.1), with 200 ml min^{-1} of humidified hydrogen (around 3% H_2O) flown at the anode side. The temperature is measured with a K thermocouple in contact with the electrolyte.

The conductivity (σ) and its error ($\Delta\sigma/\sigma$) are given by [14,15]:

$$\sigma = \frac{\ln 2}{\pi t((R_I + R_{II})/2)} \quad (1)$$

where $R_I = (\Delta U_{AB}/i_{DC})$ and $R_{II} = (\Delta U_{BC}/i_{AD})$

$$\frac{\Delta\sigma}{\sigma} = \frac{-l^2}{16d^2 \ln 2} + \frac{-L^2}{4d^2 \ln 2} \quad (2)$$

where A, B, C and D are positions of the contact around the side of the disc, t the thickness of the sample, R_I and R_{II} the measured resistance along two directions, ΔU the potential between two contacts, i the current, d the diameter of the cell, l and L the width (along the perimeter of the sample) and the length (along the radius) of the electrical contact, respectively.

The conductivity was measured 1 h after the re-reduction during subsequent RedOx cycles. No current is applied between the measurements.

2.4. Dilatometry

Pure electrolyte tape and each anode tape in green state were laminated separately to obtain a thickness of around 3–5 mm. This laminate was cut in 5 mm large and 8–10 mm long strips. The dilatometry measurements are done with a Bähr dilatometer model 402 with a platinum heated furnace under stagnant air with a 1 °C min^{-1} heating rate until 600 °C and 3 °C min^{-1} until 1400 °C for 4 h.

2.5. Microstructure observation

To preserve the microstructure during polishing, the samples were impregnated using 3 different mixtures of epoxy embedding kit (Fluka no. 45359) with acetone to lower the viscosity. The acetone to epoxy volume ratios were 3:1, 1:1 and 1:3, the samples placed successively in the different mixtures for 30 min under mild vacuum (200 mbar). Finally, the samples were immersed in pure epoxy and cured for 36 h. Polishing was done with diamond lapping films down to 1 μm with water as lubricant and cooling medium.

Scanning electron microscopy (Zeiss NVision 40 Crossbeam) equipped with a Schottky field emission gun, a Gemini column and energy selective backscattered electron detector (EsBSE) was carried out on the samples. The optimal conditions to differentiate the metallic nickel and the zirconia phases using the EsBSE detector are an accelerating voltage of 1.9 kV and slow scan. In these conditions, the BSE yield gives the contrast by opposition to other studies where the secondary electron detector is employed to differentiate the phases [16,17]. In these cases, the contrast is obtained due to the difference in surface potential of the two phases.

3. Results and discussion

3.1. Dilatometry

Dilatometry results of the anode and the electrolyte are compared in Fig. 1. Around 200 °C, tapes T50 and T60 present a small expansion; this can be observed at the temperature of softening point (T_d) of organic compounds [18]. Melting of amylose crystallite contained in the pore-former occurs at 144 °C but a complexation with other organic compounds can increase crystallite melting temperature [19]. The strong shrinkage at 300 °C is due to the decomposition of the binder and the PF; as the electrolyte contains a smaller amount of binder and no PF, the shrinkage is very small. The sintering starts around 950 °C for tapes with 50 and 60 wt% NiO and about 30 °C higher for the tape with 40 wt% NiO. The anodes shrink about 10% (of their full shrinkage) during the plateau at 1400 °C. The electrolyte shows a smoother shrinkage starting around the same temperature as the anodes, but the electrolyte reaches the sintering plateau with only 75% of its total shrinkage, that means during the plateau at 1400 °C it will still shrink about 25% of its full contraction. In comparison the anodes shrink about 10% (of their full shrinkage) during the plateau at 1400 °C. The final shrinkage is in the same range for the anodes and the electrolyte. These dilatometry measurements give us an idea of the stress and the curvature of the half cell during the debinding and the sintering [11]. To avoid cracking of the multilayer a slow debinding step is needed. To keep the half-cell flat, the green tape can be sandwiched between two ceramic plates during firing.

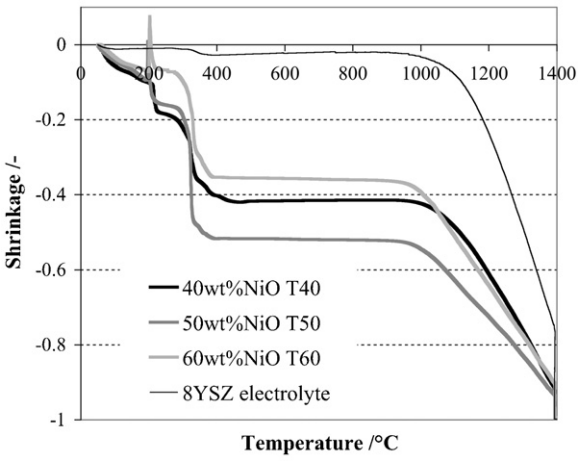

Fig. 1. Normalized linear shrinkage of the different tapes and the electrolyte versus time and temperature.

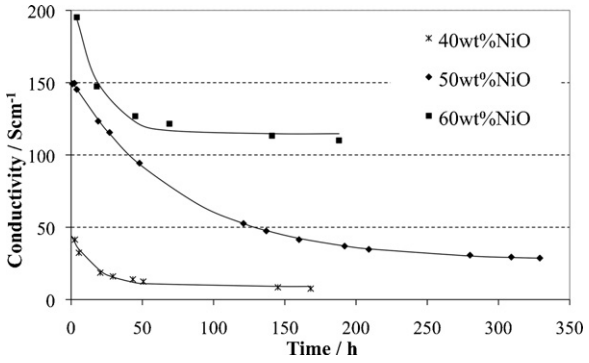

Fig. 2. Electrical conductivity versus time after the first reduction. The marks are experimental measurements and the lines are fitted to an experimental model (see Eq. (3)). Conditions: 97% H_2 + 3% H_2O at 800 °C.

3.2. Electrical conductivity

The electrical conductivity (σ) versus time is shown in Fig. 2 after the first reduction and in Fig. 3 after the RedOx treatments (10 RedOx cycles for T40 and T50 and 11 RedOx cycles for T60). σ values 1 h after each RedOx cycle is given in Fig. 4. Upon final cool down, the conductivity was measured versus the temperature, cf. Fig. 5.

In Figs. 2 and 3, the degradation of electrical conductivity with time is well fitted using an equivalent unloading capacitor model [17]:

$$\sigma(t) = (\sigma_0 - \sigma_\infty)\exp\left(-\frac{t}{\tau}\right) + \sigma_\infty \quad (3)$$

where t is time, σ the conductivity, τ the time constant and σ_0 and σ_∞ the initial and infinite time conductivity constant, respectively. The constants and the coefficient of multiple determination R^2 are

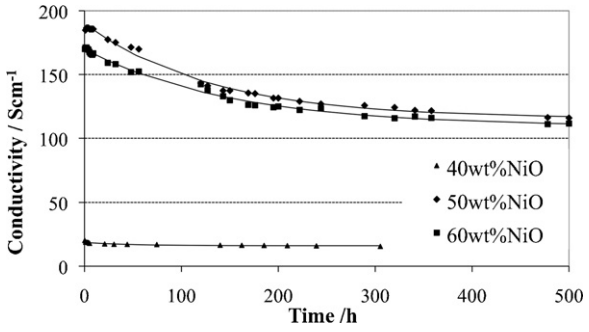

Fig. 3. Electrical conductivity versus time after multiple RedOx cycles (10 RedOx cycles for T40 and T50 and 11 RedOx cycles for T60). Conditions: 97% H_2 + 3% H_2O at 800 °C.

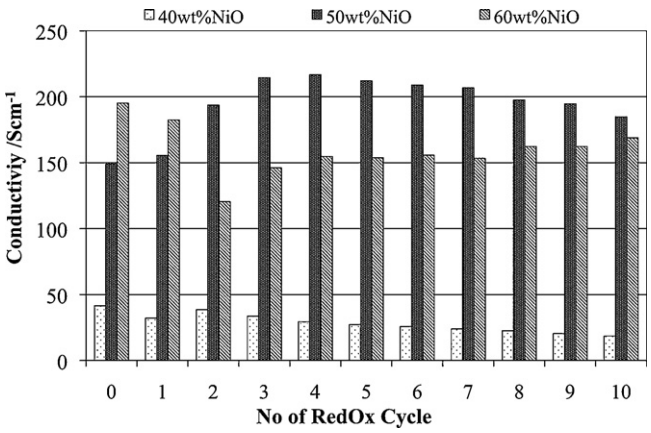

Fig. 4. Electrical conductivity versus RedOx cycles (1 h after insertion of the reducing gas). Conditions: 97% H_2 + 3% H_2O at 800 °C.

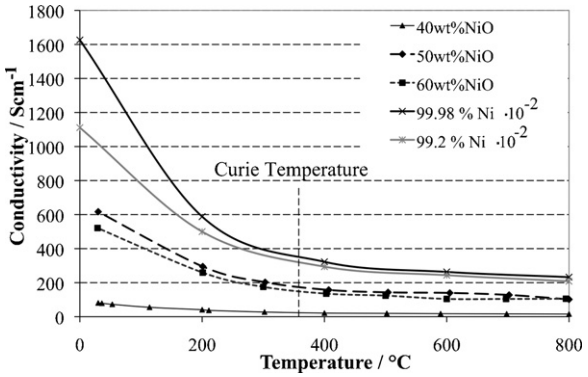

Fig. 5. Electrical conductivity versus temperature after the RedOx cycles for the cermet compared to extra pure and pure nickel from [22,23] (conductivity divided by 100). Conditions for cermet measurement: 10% H_2 + 3% H_2O + 87% N_2.

given in Table 2 for the first reduction (Fig. 2) and the reduction after multiple RedOx cycles (Fig. 3).

A similar model was used by the authors to fit the nickel particle size growth and triple phase boundary decrease in a Ni–YSZ cermet [17]. The nickel particles grow until the YSZ backbone limits their growth. The different constants depend on the cermet microstructure. The growth of Ni particle size will limit the electrical contact between particles. The same law will govern the conductivity degradation and the nickel particle size coarsening as shown in Figs. 2 and 3. σ_∞ for tape T40 (40 wt% NiO) was equal to 9 S cm^{-1} and could therefore limit the cell performance. For a 500 μm thick support, the ohmic loss due to anode resistivity alone will be ca. 6 mΩ cm^{-2}. This value is nonetheless still acceptable; a Ni rich current collecting layer could in this case be applied on the anode support.

Usually, the electrical conductivity of the cermet after a RedOx cycle is higher than before, but degrades faster, as shown by Klemensoe [20] and Grahl-Madsen et al. [21]. However, the time constant seems to increase after the RedOx cycles for the studied samples as presented in Table 2, Figs. 2 and 3. For tape T50 with 50 wt% NiO, the RedOx treatments increased the conductivity of the anode. In opposite, sample T60 lost some electrical conductivity. Disassembly of the latter cell showed this could also have been an experimental artifact.

Fig. 4 shows electrical conductivity of the three anodes after each of the 10 RedOx cycles (measurement done 1 h after each cycle). Electrical conductivity increases for tape T50 (50 wt% NiO) with each subsequent RedOx cycle until the 4th cycle and then starts to slightly decrease. For tape T60 (60 wt% NiO) the conductivity diminishes during the two first cycles, then reverts to stabilize to around 160 S cm^{-1}. Tape T40 with 40 wt% NiO shows the lowest initial value around 45 S cm^{-1}, which continuously decreases after the second RedOx cycle to reach about 20 S cm^{-1} after 10 cycles.

The electrical conductivity of anode composite decreases with temperature like for metallic materials (see Fig. 5). There is a change in $\sigma(T)$-behavior between ferromagnetic and paramagnetic nickel at the Curie temperature (between 350 and 360 °C for pure nickel [22]). The electrical conductivity is sensitive to small amounts of impurities, especially at low temperature (at room temperature around 30% lower conductivity with only 0.8% of alloying elements [23]). The nickel oxide used for the anode support fabrication is only 99.0% pure. In our cermet, some impurities can stay in oxide form, or impurities coming from the sintering or testing conditions can lower the conductivity. More analysis is required to determine the nickel purity in the cermet.

The electrical conductivity ratio between 800 °C and room temperature is 1/5th for 0.8% alloyed nickel and less than 1/6th for extra pure nickel. Experimentally, and consistent with the previous statement, we found $\sigma_{800\,°C}/\sigma_{30\,°C}$ equal to 20.5%, 16.5% and 19.2% for T60, T50 and T40, respectively. Grahl-Madsen et al. found a ratio of about 18% for a similar composite containing 55.6 wt% NiO in the ceramic mixture [21].

3.3. Electrochemical performances

Fig. 6 compares the performance of tape T40 (containing 40 wt% NiO) before and after 12 full RedOx cycles (11 RedOx at 800 °C and one at 850 °C) with the current–voltage (I–V) curves and electrochemical impedance spectroscopy (EIS) spectra at open circuit voltage (OCV) and 0.2 A cm^{-2}. The OCV value from the I–V curve is constant, which confirms the integrity of the thin electrolyte after RedOx cycling even up to 850 °C. The degradation can be quantified by different performance factors of the cell such as current density (I) or power density (P) at a certain potential (U) i.e. potentiostatic mode. Yokokawa et al. show that the degradation presented in galvanostatic mode is proportional to the current density [24] but in potentiostatic mode the degradation is independent of the current density as it degrades with the increase in ASR:

$$U_1 = U_{Nernst} - ASR_1 I_1 \quad \text{(before degradation)} \tag{4}$$

$$U_2 = U_{Nernst} - ASR_2 I_2 \quad \text{(after degradation)} \tag{5}$$

Table 2
The exponential constants and the coefficient of multiple determination, R^2, for the fit of electrical degradation presented in Figs. 2 and 3 using Eq. (3).

Sample		τ/h	σ_0/S cm^{-1}	σ_∞/S cm^{-1}	R^2
40 wt% NiO T40	Initial reduction	17.3	44.40	9.14	0.9944
50 wt% NiO T50		76.4	151.9	26.9	0.9999
60 wt% NiO T60		18.1	213.5	114.7	0.9993
40 wt% NiO T40	Reduction after 10 RedOx cycles	48.4	18.6	16.0	0.9997
50 wt% NiO T50		130.6	190.2	115.4	0.9998
60 wt% NiO T60		150.8	170.0	109.2	0.9998

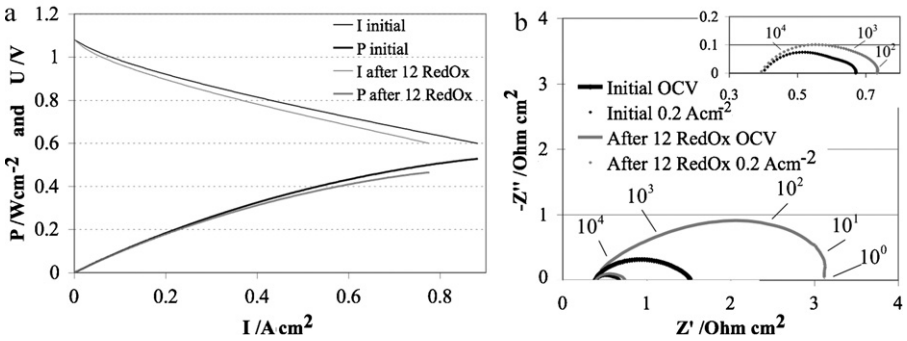

Fig. 6. Comparison of the performance of 40 wt% NiO tape before and after 12 RedOx cycles with (a) current–voltage (*I–V*) and current–power (*I–P*) curves and (b) electrochemical impedance spectroscopy at open circuit voltage (OCV) and 0.2 A cm^{-2}. Conditions: 97% H_2 + 3% H_2O at 800 °C.

With $U_1 = U_2$ in potentiostatic mode, then

$$\frac{I_1}{I_2} = \frac{ASR_2}{ASR_1} \tag{6}$$

Then the degradation is defined as:

$$\text{Degradation}/\% = \frac{I_2 - I_1}{I_1} = \frac{I_2}{I_1} - 1 = \frac{ASR_1}{ASR_2} - 1 = \frac{ASR_1 - ASR_2}{ASR_2} \tag{7}$$

In the potentiostatic mode the degradation can be taken from the current density at a certain constant potential or the power density at the same potential and this will be independent of the current as it decreases inversely to the ASR increase. This approach is only valid at low fuel utilization (F_u) with humidified fuel where the Nernst potential does not vary with current density. In the case of the T40 sample at 0.65 V, the current varies from 0.763 to 0.669 A cm^{-2} (see Table 3) during the degradation; this corresponds to 1.8 and 1.6% of F_u and 1.081 and 1.079 V for the calculated Nernst potential for 300 ml min^{-1} cm^{-2} of 97% H_2 and 3% H_2O.

The slope of the *I–V* curve gives the area specific resistance (ASR). This value can be calculated from the *I–V* curve between two measured points or extracted from the EIS spectra at the maximal real impedance (with $Z'' = 0\ \Omega\ cm^2$). The degradation of tape T40 through 12 RedOx cycles is quantified with these different methods and compared in Table 3. The different methods to express degradation give consistent values of around 1% loss per cycle, except for ASR evolution from the EIS measurements at OCV. The impedance was measured with a 30 mA current amplitude. At OCV, the cell works in fuel cell mode or in electrolyzer mode depending on the direction of the current. This measure is very sensitive to the water vapor content of the anode gas. Without water in the fuel, the electrolyzer mode is strongly limited, as shown by a conversion arc at low frequency [24]. During the measurements, hydrogen was humidified at room temperature, to give about 3% H_2O. Thus EIS measurement at OCV is not recommended to measure performance degradation as it depends strongly on the water vapor partial pressure in the fuel gas. The other methods gave similar values for the degradation extent. Depending on the shape variation of the *I–V* curve during successive RedOx cycles, the ASR method or the output current density method will give slightly different results. Therefore in the following graphs both ASR and current density are given.

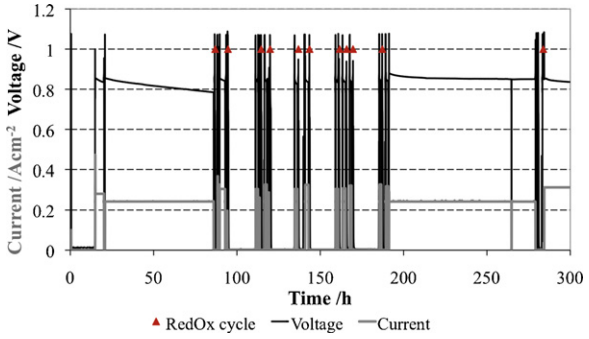

Fig. 7. Tape T60 (60 wt% NiO) cell potential and current density versus time. RedOx cycles are represented by triangles. A drop in potential occurs after each RedOx cycle, *I–V* curve and EIS measurement. Reduction conditions: 97% H_2 + 3% H_2O, oxidation conditions: dry air.

In Fig. 7, an example of raw data measurement for anode tape T60 (60 wt% NiO) is presented. This graph shows the cell potential and current density versus time. Each triangle represents a RedOx cycle. A drop in potential occurs after each RedOx cycle, *I–V* curve and EIS measurement. As for tape T50, the OCV is constant after each RedOx cycle. The first degradation of potential at constant current (from 20 h to 80 h) seems not to stabilize during the 60 h of testing. After 10 RedOx cycles (from 190 h to 280 h), the potential seems to stabilize at a higher level after ca. 10 h. The cell performance appears more stable after the RedOx treatment than before. For a simple direct performance comparison of the three anodes, Figs. 8–10 show their OCV, current density at 0.6 V and ASR (between 0.65 and 0.85 V) versus the RedOx cycles.

For the 3 compositions, the OCV is stable upon RedOx cycling, indicating that the expansion is lower than the critical support expansion of 0.2% [3,7]. In Part I of this study, the composition and microstructure of the different supports was optimized through a

Table 3
Comparison of degradation measurements of T40 using different values of current density, *I*, at potential, *U*, of 0.65 V and 0.85 V and area specific resistance, ASR, at and between these values and using electrochemical impedance spectroscopy (EIS) at open circuit voltage (OCV) and 0.2 A cm^{-2}. Degradation equals to $(I_2 - I_1)/I_1$ or $(ASR_1 - ASR_2)/ASR_2$ with subscripts 1 and 2 corresponding before and after the degradation, respectively.

		Initial performance		After 12 RedOx cycles		Degradation per cycle	
	U/V	*I*/A cm^{-2}	ASR/Ω cm^2	*I*/A cm^{-2}	ASR/Ω cm^2	*I*	ASR
IV	0.85	0.328	0.518	0.275	0.581	−1.3%	−0.9%
IV	0.65	0.763	0.424	0.669	0.467	−1.0%	−0.8%
IV	0.85–0.65		0.460		0.508		−0.8%
EIS	OCV		1.51		3.12		−4.3%
EIS		0.2	0.673	0.2	0.734		−0.7%

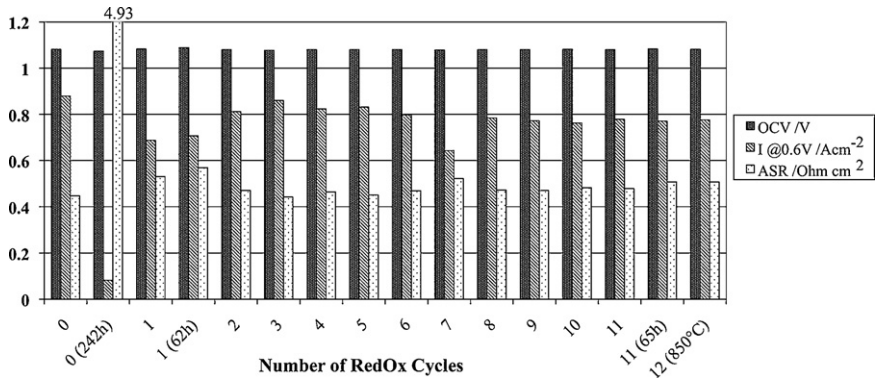

Fig. 8. Open circuit voltage (OCV), current density (I) at 0.6 V and area specific resistance (ASR) of tape T40 containing 40 wt% NiO with the number of RedOx cycles. Conditions: 97% H_2 + 3% H_2O at 800 °C. Measurement done 1 h after re-reduction when not stated.

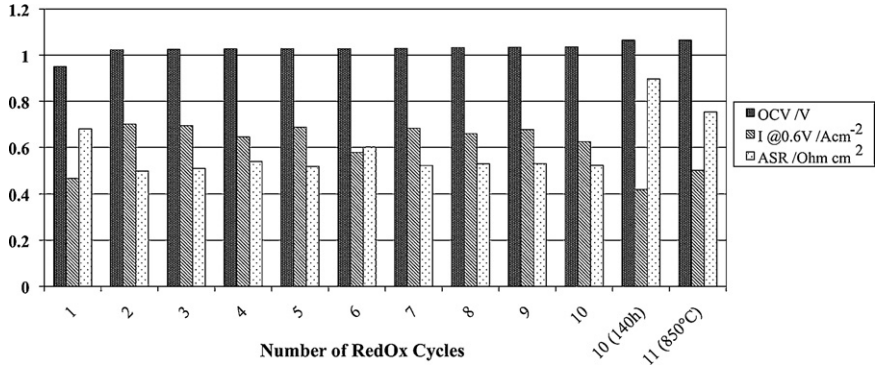

Fig. 9. Open circuit voltage (OCV), current density (I) at 0.6 V and area specific resistance (ASR) of tape T50 containing 50 wt% NiO with the number of RedOx cycles. Conditions: 97% H_2 + 3% H_2O at 800 °C.

design of experiment approach to lead to RedOx stable anodes with reasonable conductivity and sinterability [10]. The electrochemical performance of the anode, however, was not yet optimized. The mean value for current density at 0.6 V is between 0.6 and 0.8 A cm^{-2} for the three compositions. The best performance is for T60 with an initial performance of 1.15 A cm^{-2} at 0.6 V dropping to around 0.8 A cm^{-2} after RedOx cycling. The lowest performance is for T50. This anode contained 5% of coarse NiO powder, which can limit its performance. The cell from T40 underwent an accidental, uncontrolled RedOx cycle before measurement. Its initial OCV was lower, but increased with time and RedOx cycle. The lower initial OCV could come from the accidental RedOx cycle or from pinholes in the as sintered electrolyte. It has been shown that a small electrolyte crack can heal during utilization [3]; this could explain the increase of OCV during the testing time.

After 10 RedOx cycles at 800 °C, the cells were polarized longer before the last RedOx cycle at 850 °C. For the anode T40 in Fig. 8, the degradation 242 h after the first reduction is huge, the current density degrades more than 90% over this period giving a degradation rate of 37.5%/100 h. After the RedOx treatments the degradation over 65 h is less than 1.0% giving a degradation rate of 1.5%/100 h. A similar observation applies to the T60 cell (Fig. 10), the first reduction giving a degradation rate of 72%/100 h, which drops to 13%/100 h after the RedOx treatments. The conductivity measurements present similar results: the decrease of conductivity is faster during the first reduction than after RedOx cycles.

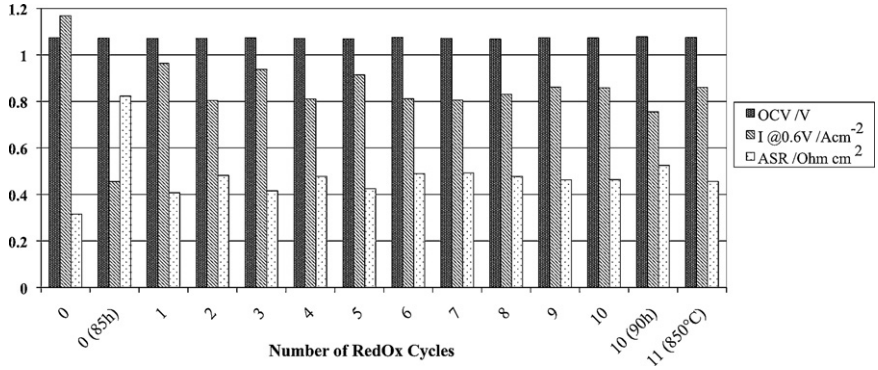

Fig. 10. Open circuit voltage (OCV), current density (I) at 0.6 V and area specific resistance (ASR) of tape T60 containing 60 wt% NiO with the number of RedOx cycles. Conditions: 97% H_2 + 3% H_2O at 800 °C.

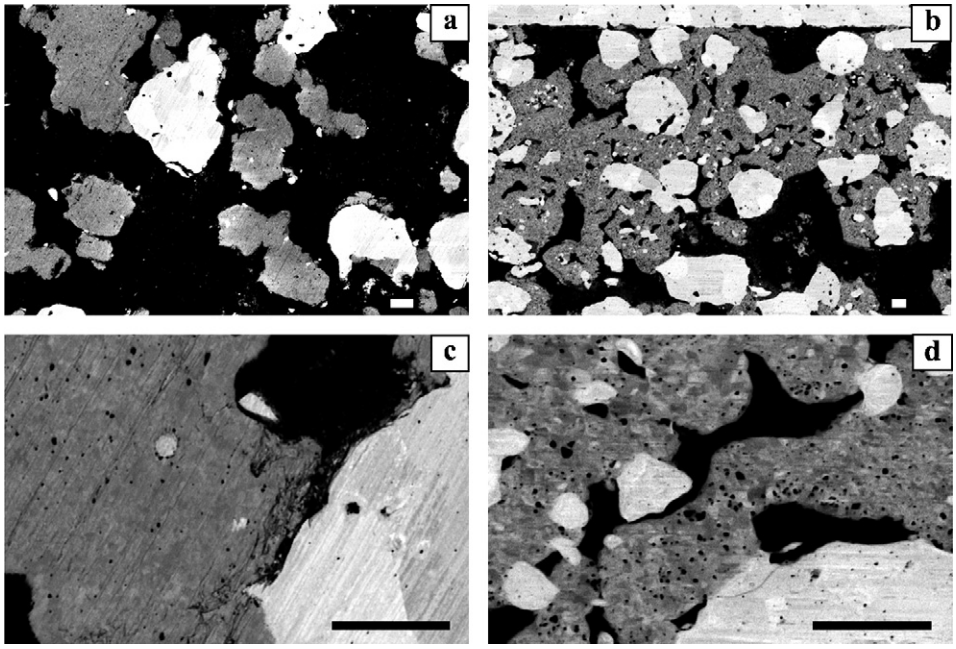

Fig. 11. Anode containing 60 wt% NiO after 300 h at 800 °C under humidified formier gas (10% H_2 in N_2) (a) and (c) fresh as-sintered sample and (b) and (d) tested sample. The grey levels separate each phase (YSZ: light grey, Ni: dark grey and porosity: black). All data-bars are 2 μm in length.

3.4. Microstructural characterization

To understand the lower degradation after the RedOx treatments, the microstructure of fresh samples reduced 300 h at 800 °C is compared to tested samples (from Fig. 10) reduced in similar conditions. The micrographs of T60 anodes are presented in Fig. 11 (the other tapes present similar microstructures but are not shown here). The microstructure of such samples is coarse compared to other so-called standard anodes [17,25]. The goal of the present microstructure was to contain enough porosity for RedOx stability, and not yet to be optimized for high electrochemical performance. The coarse YSZ powder increases the porosity by reducing the sintering shrinkage of the anode [10]. 300 h after the first reduction, the nickel grains (in dark grey) are round and rather separated from each other (Fig. 11a), which is bad for the percolation of the electrically conducting phase. The nickel grains coalesce during prolonged periods at working temperature and under reducing atmosphere even if the original NiO powder is fine [17,25]. The YSZ backbone should stop the nickel grains coarsening [17]. In our case, the high porosity and coarse YSZ backbone cannot limit the nickel coalescence. This is the reason of the rapid decrease of conductivity and electrochemical performance, during steady state operating conditions after first reduction, especially for samples containing less NiO.

The samples that underwent the 11 RedOx cycles show a very different microstructure (Fig. 11b). The nickel grains contain microporosities that increase the nickel volume and so give a percolating structure. The closed porosity in the nickel grains comes from the previous re-oxidation of the metallic phase. As known from bulk nickel oxidation, the diffusion coefficient in the NiO layer is higher for Ni^{2+} than for O^{2-} ions [26]. This creates an internal porosity due to the outward diffusion of nickel through the NiO shell during oxidation [27]. In a YSZ–Ni cermet, the pore size increases with enhanced temperature of oxidation [3]. The interesting observation of Fig. 11b is the stability of this porosity over long reduction periods. The reason could come from the small YSZ particles broken during the RedOx cycles and included in the nickel grains (see Fig. 11b and d). Due to the high contact angle between YSZ and Ni (117° [28]), these small ceramic particles slow down the agglomeration and densification of the nickel phase. Porosity is very often found near YSZ particles in Fig. 11d. At higher magnification (Fig. 11c and d), nano-porosity is observed in both the YSZ and Ni phases. Nano-porosities are reported for transmission electron microscopy samples from anode cermets after *ex-situ* and *in-situ* reduction [9,29]. Nano-porosities are more present in the nickel phase from the sample after RedOx treatment than in that from the sample after only one reduction. This nano-porosity can also increase the volume of the electrically conducting phase and so increase its percolation. Further observations and studies have to confirm the presence of this nano-porosity in bulk samples.

These microstructural observations can clarify the difference in behavior between standard and high porosity anode supports. For a standard anode support, the electrical conductivity after a RedOx cycle is higher but degrades faster [20,21], the expansion is not reversible and increases after each cycle [20]. That means, the nickel expansion during re-oxidation breaks the YSZ backbone. After re-reduction, the anode porosity increases due to the irreversible expansion. This diminishes the percolation of the conducting phase when the nickel is fully reduced and starts to coalesce. A high porosity anode support is mechanically sufficiently stable to keep the OCV constant (expansion lower than 0.2%). Its microstructural change is only a reorganization of the nickel phase inside the YSZ backbone, which is in favor for the nickel percolation (see Fig. 11).

3.5. Comparison of tape-cast sample with design of experiment prediction

Table 4 presents the results of the samples prepared by tape-casting with the design of experiment prediction, which was based on samples produced by isostatic powder compaction. Linear shrinkage and porosity are higher for tape-cast samples. First, this can be explained by the higher content of binder and dispersant for samples prepared by tape-casting. The 20.3 wt% of organic binder and dispersant represent 58.9 vol% in the green state after drying. The samples produced by dry isostatic pressing contain only 1.04 wt% of organics (stearic acid and acrylic binder) that repre-

Table 4
Comparison of tape-cast samples with the predictions done by the surface response model proposed in [10].

	Tape T40	Tape T50	Tape T60
Samples from tape-casting, this study			
Linear shrinkage after firing /%	−14.0 ± 0.6	−13.4 ± 0.6	−16.0 ± 0.9
Porosity as-sintered /%	46.8 ± 2.4	50.1 ± 3.2	51.7 ± 1.1
Vol% of organics in green state /vol%	60.9	63.7	64.8
Electrical conductivity after 24 h of reduction calculated for room temperature /S cm^{-1}	97.7 ± 1.1	645 ± 12	770 ± 7
Values from design of experiment model, Part I [10]			
Linear shrinkage after firing /%	−7.3	−9.6	−9.1
Porosity as-sintered /%	23.3	27.9	32.9
Vol% of organics in green state /vol%	15.9	27.2	30.6
Electrical conductivity after 24 h of reduction /S cm^{-1}	1554	2402	3247
1st RedOx strain /%	0.1	0.16	0.03

sent 6.5 vol% in the green state [10]. In Table 4, the organic content includes also the pore-former volume. Second, the samples used for the optimization study are pressed isostatically at 200 MPa during 1 min before firing. This compaction can remove the remnant porosity in the green state. The tape-cast sample compaction is only done during drying (no pressure added). Finally, the dry ball-milling which was performed for powders used to press samples can break the powder due to the higher applied energy. This can change the firing process and the final microstructure.

The electrical conductivity of sintered samples from cast tapes is calculated for room temperature (T_r), so they can be compared to the powder compact samples (measured at T_r). The value obtained at 800 °C after 24 h of reduction was multiplied by the ratio of electrical conductivity at T_r versus 800 °C ($\sigma_{Tr}/\sigma_{800\,°C} \approx 5.45$) for all samples. The conductivity is lower for the tape-cast samples due to their higher porosity compared to the pressed samples. If the tape-cast samples are analyzed using the conductivity model developed in [10]:

$$\sigma_{comp} = (1 - p_{pore})^{q/\nu_{Ni}} \sigma_{eff} \quad (8)$$

with $\sigma_{eff} = \nu_{Ni}\sigma_{Ni} + \nu_{YSZ}\sigma_{YSZ}$ where σ_i are the electrical conductivities of the composite and the different phases, ν_{Ni} and ν_{YSZ} are the Ni and the YSZ volume fraction in the solid phase, p_{pore} is the porosity proportion and q is a constant. To fit the conductivity of the tape-cast samples with the model, the constant q varies between 1.64 for tape T50 and 1.95 for tape T60. The value for the pressed samples is 1.83 (42 samples, $R^2 = 0.97$). This confirms that the difference in electrical conductivity between pressed and tape-cast samples is mostly due to the variation in porosity of the samples.

The principal goal of the study was reached. The strain obtained after RedOx cycles is lower than the critical value for electrolyte integrity (calculated around 0.2% [3,7]). This was shown for the different samples produced by tape-casting by the constant OCV during subsequent RedOx cycles. The value from the surface response model is lower than the 0.2% limit (see Table 4). It is interesting to note that the porosity of the tape-cast samples is around 50%, which was defined as a safety limit for RedOx stability [10].

4. Conclusion

A design of experiment procedure was used to suggest and fabricate new SOFC anode support microstructures with RedOx stability.

Three different anode compositions based on 40, 50 and 60 wt% NiO were characterized by conductivity and electrochemical measurements with time, and undergoing 10 full RedOx cycles at 800 °C plus one full RedOx cycle at 850 °C.

The electrical conductivity degrades with time and can be fitted by an exponential model. This could be related to nickel phase coarsening. After RedOx treatments this degradation is slower due to a re-organization and a stabilization of the nickel phase. The conductivity of the anode can increase or decrease with the consecutive RedOx cycles depending on the microstructure and composition.

The open circuit voltage was stable for all 11 RedOx cycles showing that the electrolyte survives the treatments and that the expansion of the support during re-oxidation is lower than the 0.2% critical limit.

Similar to the conductivity behavior, the electrochemical performances degrade faster after the first reduction than after RedOx cycles. Microstructure observations on non-reoxidized samples show spherical nickel grains 300 h after the first (and only) reduction. For samples that underwent 11 RedOx cycles, however, the nickel phase contains small zirconia fragments and a stable micro-porosity. The internal micro-porosity is known to be due to the Ni oxidation process. YSZ fragments produced during RedOx cycling stabilize the nickel internal porosity. The foamy nickel microstructure increases the percolation of the electrical conducting phase. The change in nickel microstructure during re-oxidation reactivates the degraded anode. This process can be used to restore the performance of a Ni–YSZ anode after continuous degradation.

For samples with 40 and 60 wt% of NiO, the electrochemical performances were stable after the second RedOx cycle at 800 °C. These results are promising for future cells with increased size.

Acknowledgements

Kind acknowledgements are extended to the Ceramic Laboratory (Prof. N. Setter and J. Castano) for the furnace and cell fabrication facilities and to the European Institute for Energy Research (EIfER, Karlsruhe, Germany) for the financial support (contract no. N43/C06/019), as well as to the European Commission for funding of the FP7 project RobAnode (grant agreement 245355).

References

[1] Z. Wuillemin, N. Autissier, M. Nakajo, M. Luong, J. Van herle, D. Favrat, J. Fuel Cell Sci. Technol. 5 (2008) 0110161–0110169.
[2] Z. Wuillemin, A. Faes, S. Diethelm, A. Nakajo, N. Autissier, J. Van herle, D. Favrat, in: U. Bossel (Ed.), 8th European Solid Oxide Fuel Cell Forum, Lucerne, Switzerland, 2008, p. P0224.
[3] A. Faes, A. Nakajo, A. Hessler-Wyser, D. Dubois, S. Modena, A. Brisse, J. Van herle, J. Power Sources 193 (2009) 55–64.
[4] D. Larrain, J. Van herle, D. Favrat, J. Power Sources 161 (2006) 392–403.
[5] J.P. Ouweltjes, M. Van Tuel, M. Sillessen, G. Rietveld, Fuel Cells 9 (2009) 873–882.
[6] B. Iwanschitz, J. Sfeir, A. Mai, M. Schotze, J. Electrochem. Soc. 157 (2010).
[7] D. Sarantaridis, A. Atkinson, in: U. Bossel (Ed.), 7th European Solid Oxide Fuel Cell Forum, Lucerne, Switzerland, 2006, p. P0728.
[8] G. Robert, A. Kaiser, E. Batawi, in: M. Mogensen (Ed.), 6th European Solid Oxide Fuel Cell Forum, Lucerne, Switzerland, 2004, p. 193.
[9] D. Waldbillig, A. Wood, D.G. Ivey, J. Power Sources 145 (2005) 206–215.
[10] A. Faes, J.M. Fuerbringer, D. Mohamedi, A. Hessler-Wyser, G. Caboche, J. Van herle, J. Power Sources (2010), doi:10.1016/j.jpowsour.2010.07.092.
[11] M. Cologna, A.R. Contino, D. Montinaro, V.M. Sglavo, J. Power Sources 193 (2009) 80–85.
[12] P. Tanasini, P. Costamagna, M. Cannarozzo, A. Faes, A. Hessler-Wyser, J. Van herle, C. Comninellis, Fuel Cells 9 (2009) 740–752.
[13] A. Mai, B. Iwanschitz, R. Denzler, D. Haberstock, A. Schuler, in: P. Connor (Ed.), 9th European Solid Oxide Fuel Cell Forum, Lucerne, Switzerland, 2010, pp. 2–144.

[14] J.L. Van der Pauw, Philips Res. Rep. 13 (1958) 1–9.
[15] J. Van herle, A.J. McEvoy, K.R. Thampi, J. Mater. Sci. 29 (1994) 3691–3701.
[16] K. Thyden, Y.L. Liu, J.B. Bilde-Soerensen, Solid State Ionics 178 (2008) 1984–1989.
[17] A. Faes, A. Hessler-Wyser, D. Presvytes, C.G. Vayenas, J. Van herle, Fuel Cells 9 (2009) 841–851.
[18] M.J. Edirisinghe, J.R.G. Evans, J. Mater. Sci. 22 (1987) 2267–2273.
[19] Z.Q. Liu, A.M. Cunha, X.S. Yi, C.A. Bernardo, J. Macromol. Sci.: Phys. 40B (2001) 529–538.
[20] T. Klemensoe, Technical University of Danemark, Risoe National Laboratory, Topsoe Fuel Cell, 2005.
[21] L. Grahl-Madsen, P.H. Larsen, N. Bonanos, J. Engell, S. Linderoth, J. Mater. Sci. 41 (2006) 1097–1107.
[22] S.J. Rosenberg, Nickel and its Alloys, National Bureau of Standard, U.S. Government, Washington, 1968.
[23] H.G. Isabellenhütte, Dillenburg, Germany, 2010. Available from: http://www.isabellenhuette.de/pdf/WIDER_LEG/SUPER-PURE-NICKEL-ISABELLENHUETTE-R.pdf.
[24] H. Yokokawa, H. Tu, B. Iwanschitz, A. Mai, J. Power Sources 182 (2008) 400–412.
[25] D. Simwonis, F. Tietz, D. Stoever, Solid State Ionics 132 (2000) 241–251.
[26] A. Atkinson, R.I. Taylor, J. Mater. Sci. 13 (1978) 427–432.
[27] D. Sarantaridis, R.J. Chater, A. Atkinson, J. Electrochem. Soc. 155 (2008) B467–B472.
[28] A. Tsoga, A. Naoumidis, P. Nikolopoulos, Acta Mater. 44 (1996) 3679–3692.
[29] A. Faes, Q. Jeangros, J.B. Wagner, T.W. Hansen, J. Van herle, A. Brisse, R. Dunin-Borkowski, A. Hessler-Wyser, ECS Trans. 25 (2009) 1985–1992.